nature communications

Article

https://doi.org/10.1038/s41467-026-69338-8

A medium-entropy oxygen electrode enables high-performance and contaminant-tolerant reversible solid oxide cells

Received: 12 June 2025

Accepted: 29 January 2026

Published online: 11 February 2026

Check for updates

Feng Zhu, Kang Xu, Yuhe Liao, Liyan Chen, Yangsen Xu, Feng Hu, Fan He, Xirui Zhang & Yu Chen

The development of oxygen electrodes with sufficient oxygen reduction reaction (ORR) and oxygen evolution reaction (OER) activity, as well as good tolerance to contaminants, is crucial for promoting the commercialization of reversible solid oxide cells (Re-SOCs) technologies. Herein, we design and synthesize a medium-entropy oxygen electrode with a formula of $Pr_{0.5}Ba_{0.2}Sr_{0.2}Ca_{0.1}CoO_{3-\delta}$ (ME-PBSCC). The abundant surface oxygen vacancy concentration, high electrical conductivity, rapid and stable oxygen exchange kinetics, and structural stability of the ME-PBSCC oxygen electrode ensure the efficient and poisoning-tolerant ORR/OER in ambient air and Cr-contaminated atmosphere. Specifically, Re-SOCs incorporating the PBSCC oxygen electrodes exhibit maximum power densities of 2.239 (in ambient air) and 1.859 W cm^{-2} (in a Cr-contaminated air) at 750 °C in fuel cell (FC) mode, and current densities of 1.10 A cm^{-2} at 1.3 V and 700 °C under 50% H_2O (in a Cr-contaminated air) in electrolysis (EC) mode, demonstrating competitive performance for Re-SOCs. More importantly, the developed ME-PBSCC oxygen electrode has achieved the highly promising stable operation of Re-SOCs in FC, EC, and reversible modes in the presence of Cr contamination.

Since the Industrial Revolution, the large-scale utilization of fossil fuels has significantly propelled the development of human society. However, it has also led to a series of issues, including resource depletion, environmental pollution, and climate change[1,2]. Innovating and efficient utilization of renewable and clean resources constitutes a critical pathway to alleviate the current predicament[3,4]. Among the various energy storage and conversion technologies, reversible solid oxide cells (Re-SOCs) have garnered increasing attention during the past several decades, potentially aiding the realization of low or zero carbon emissions[5,6]. In particular, Re-SOCs can be operated in fuel cell (FC) mode to generate electricity and in electrolysis (EC) mode to store energy, thus having the potential capability of peak shaving and valley filling, and long-term energy storage[7,8].

One of the crucial challenges to the commercial viability of Re-SOCs is the sluggish kinetics of oxygen reduction reaction (ORR) and oxygen evolution reaction (OER) at oxygen electrodes at intermediate temperatures (IT), resulting in unsatisfactory electrochemical performance[9]. An ideal oxygen electrode material for IT-Re-SOCs should possess high ionic and electronic conductivity, stable phase structure, excellent chemical compatibility with typical electrolyte materials, and sufficient tolerance to contaminant poisoning (such as carbon dioxide, water vapor, and volatile Cr-containing vapor, etc.), which ensures the efficient and stable ORR/OER[10]. Unfortunately, although significant progress has been achieved in the development of promising oxygen electrodes for Re-SOCs, most of the electrochemical results obtained are based on relatively mild experimental conditions[7,11–14]. Under realistic operating conditions, the oxygen electrodes of cell stacks inevitably encounter harsh atmospheres[15]. For instance, gaseous Cr species volatilize from the Cr_2O_3 scale of metallic alloy interconnects, which are employed for electrical connections between individual cells and gas transport channels isolating the fuel electrode and the oxygen electrode[16]. Specifically, high-valent Cr

School of Environment and Energy, South China University of Technology, Guangzhou, China. e-mail: eschenyu@scut.edu.cn

species (e.g., representative CrO_3 and $CrO_2(OH)_2$ in wet air) react with the alkaline-earth metal oxides segregated from the oxygen electrode to form inactive chromates, which are further deposited on the surface of the oxygen electrode or at the interface between the oxygen electrode and electrolyte[17]. On the one hand, the elemental segregation driven by the minimization of elastic energy and the electrostatic interactions alters the stoichiometry in the near-surface region of the oxygen electrode, resulting in different energy barriers for oxygen transport[18]. On the other hand, the deposited chromates with relatively low electrical conductivity (e.g., 2.00×10^{-5} S cm^{-1} of $SrCrO_4$ and 5.14×10^{-4} S cm^{-1} of $BaCrO_4$ at 700 °C, respectively)[19,20] and significant surface coverage, severely hinder electron conduction and oxygen exchange at the active sites of the oxygen electrode during ORR and OER. More seriously, gaseous Cr species may directly react with the oxygen electrode, causing Cr to enter the perovskite lattice[21]. It is reported that Cr from volatile Cr species entered the perovskite lattice of $LaNi_{0.6}Fe_{0.4}O_3$, leading to a decrease in electronic conductivity[21].

A variety of feasible strategies have been employed to alleviate Cr poisoning on oxygen electrodes, such as adding protective coatings to interconnects[22–24], placing Cr getters in the upstream airflow[25,26], and surface modification and composition optimization of the oxygen electrodes[14,27–29]. Protective coatings can effectively inhibit the growth of Cr_2O_3 scale on the interconnect and block the outward volatilization of Cr species, mainly including reactive element oxide (e.g., La, Ce, and Y oxides), metal/alloy (e.g., Co, Ni, Cu, and $NiFe_2$), spinel (e.g., $(Mn,Co)_3O_4$, $(Mn,Cu)_3O_4$, $Mn_{1.25}Co_{1.5}Cu_{0.25}O_4$, and $CuFe_2O_4$), and perovskite (e.g., $La_{1-x}Sr_xCoO_3$ and $La_{1-x}Sr_xMnO_3$) coatings[30–33]. For instance, the $(Mn,Cr)_3O_4$ layer that formed on top of the Cr_2O_3 scale was the key factor enabling the $La_{0.75}Sr_{0.25}Cr_{0.5}Mn_{0.5}O_3$ coating to block Cr diffusion[34]. The $CuMn_{1.8}O_4$ coatings reduced the Cr volatilization by reacting with the Cr_2O_3 scale to form $(Cu,Mn,Cr)_{3-x}O_4$ cubic spinel phases[35]. However, the interdiffusion of elements and mismatched thermal expansion coefficients may cause delamination and cracking of the external coating. Different preparation methods can also affect the effectiveness of protective coatings[36]. Moreover, the application of protective coatings to balance-of-plant components, which likewise constitute significant sources of Cr contamination, cannot always be readily achievable. Cr getters (such as $Sr_xNi_yO_z$ and $SrMnO_3$) are typically fabricated by combining SrO with transition metal oxides and then loaded on ceramic supports, offering another effective route for mitigating Cr poisoning on oxygen electrodes[26,37]. Among them, SrO functions as the effective component, capturing gaseous Cr species and converting them into the thermodynamically stable solid $SrCrO_4$. However, during long-term operation, the getter will inevitably become saturated with Cr deposits, necessitating frequent replenishment or replacement[31]. Therefore, in light of the above constraints, the development of oxygen electrodes that are tolerant to Cr contamination represents the fundamental solution to the poisoning.

Surface modification is one of the effective strategies to enhance the electrocatalytic activity and Cr tolerance of oxygen electrodes[38–40]. The nano-structured catalysts can increase the active sites of oxygen reactions and protect oxygen electrodes from being poisoned by contaminants. However, achieving commercially feasible, reproducible, and uniformly distributed surface modification in large-area cells with porous oxygen electrodes remains highly challenging[41]. Moreover, most reported catalysts exist as isolated nanoparticles on the oxygen electrode surface, making it difficult to achieve effective protection for the intrinsically fragile electrode under prolonged Cr exposure[38,42].

Recently, high/medium-entropy oxides have attracted extensive attention in improving the structural stability (e.g., inhibiting phase transition or elemental segregation), electrocatalytic performance, and poisoning resistance of oxygen electrodes for Re-SOCs[11,12,14,43]. On the one hand, increasing the configurational entropy (S_{config}) could overcome the phase separation driven by enthalpy, especially during high-temperature synthesis and operation, that is, entropy-dominated stabilization[44,45]. On the other hand, the lattice distortion effect of high/medium-entropy oxides, resulting from irregular distribution of doped cations with varying ionic radii, may affect the physicochemical properties of the oxides[46]. For example, Yang et al.[47] developed a high-entropy oxide $La_{0.2}Pr_{0.2}Nd_{0.2}Sm_{0.2}Sr_{0.2}MnO_{3-\delta}$ (S_{config} = 1.609R) based on $La_{0.8}Sr_{0.2}MnO_{3-\delta}$. The significant dispersion of A-site ions formed a disordered stress field around Sr, suppressing the surface migration of Sr[47]. Furthermore, a medium-entropy $SrCo_{0.5}Fe_{0.2}Ti_{0.1}Ta_{0.1}Nb_{0.1}O_{3-\delta}$ oxygen electrode (S_{config} = 1.359R) was constructed by Gao et al.[48], demonstrating better activity and stability for ORR than the benchmark $SrCo_{0.9}Ta_{0.1}O_{3-\delta}$ (S_{config} = 0.325R) under Cr-containing atmosphere. Additionally, other advanced high/medium-entropy oxygen electrodes, including $La_{0.2}Pr_{0.2}Nd_{0.2}Sm_{0.2}Gd_{0.2}BaFe_2O_{5+\delta}$[43], $(La_{0.2}Sr_{0.2}Pr_{0.2}Y_{0.2}Ba_{0.2})Co_{0.2}Fe_{0.8}O_{3-\delta}$[49], $Pr_{0.2}Sm_{0.2}Nd_{0.2}Gd_{0.2}La_{0.2}BaCo_2O_{5+\delta}$ (PSNGLBC)[14], and $Ba_{0.4}Nd_{0.1}Sr_{0.5}Co_{0.6}Ni_{0.1}Zr_{0.1}Fe_{0.2}O_{3-\delta}$[50] have also demonstrated excellent ORR activity and Cr tolerance. Regrettably, while the developed oxygen electrodes so far have achieved efficient and stable ORR in FC mode in the presence of Cr contamination, there is scant research on their effectiveness for OER in EC and reversible mode under such contamination. On the one hand, the OER during EC or reversible operation creates a more oxidized atmosphere at the oxygen electrode, which may intensify elemental segregation[51]. On the other hand, the elevated oxygen partial pressure may promote the volatilization of gaseous Cr species from the Cr_2O_3 scale. Therefore, it is also necessary to enhance the tolerance of oxygen electrodes against Cr poisoning in both EC and reversible modes.

Motivated by the aforementioned investigations, here we present a medium-entropy oxide, $Pr_{0.5}Ba_{0.2}Sr_{0.2}Ca_{0.1}CoO_{3-\delta}$ (ME-PBSCC, S_{config} = 1.221R), as a highly active, durable, and Cr-tolerant oxygen electrode material for Re-SOCs, which displays exceptional electrochemical performance and promising stability in the absence and presence of Cr contamination. The abundant surface oxygen vacancy concentration, high electrical conductivity, and rapid and stable oxygen exchange kinetics of ME-PBSCC oxygen electrode ensure the efficient and poisoning-tolerant ORR/OER. Moreover, the enhanced structural stability and chemical compatibility of ME-PBSCC towards Cr contamination have been confirmed by detailed analyses such as X-ray diffraction (XRD), scanning electron microscopy (SEM), and Raman spectroscopy. The Re-SOCs with ME-PBSCC oxygen electrodes exhibit impressive maximum power densities (P_{max}, 2.239 and 1.859 W cm^{-2} at 750 °C in the presence of ambient air and Cr contamination, respectively) in FC mode and outstanding water electrolysis current densities (1.10 A cm^{-2} at 1.3 V and 700 °C under 50% H_2O humidified H_2 in the presence of Cr contamination) in EC mode, demonstrating competitive performance for Re-SOCs. Furthermore, the good operating stabilities of Re-SOCs with ME-PBSCC oxygen electrode are also demonstrated in both FC and EC modes at 700 °C with/without Cr contaminants. Significantly, we have reported the highly promising reversible operation stability (25 cycles) of Re-SOCs with ME-PBSCC at 700 °C in the presence of Cr contamination. This work represents an important progress in developing high-performance and contaminant-tolerant oxygen electrode materials, which may contribute to the accelerated commercialization of Re-SOCs technologies.

Results

Structural and physicochemical characterizations of the ME-PBSCC

The crystalline properties of as-synthesized ME-PBSCC were analyzed using XRD along with Rietveld refinement and high-resolution transmission electron microscopy (HR-TEM) equipped with energy dispersive X-ray spectroscopy (EDX). As displayed in Fig. 1a, the ME-PBSCC exhibited a monoclinic perovskite structure (space group P21/

https://doi.org/10.1038/s41467-026-69338-8

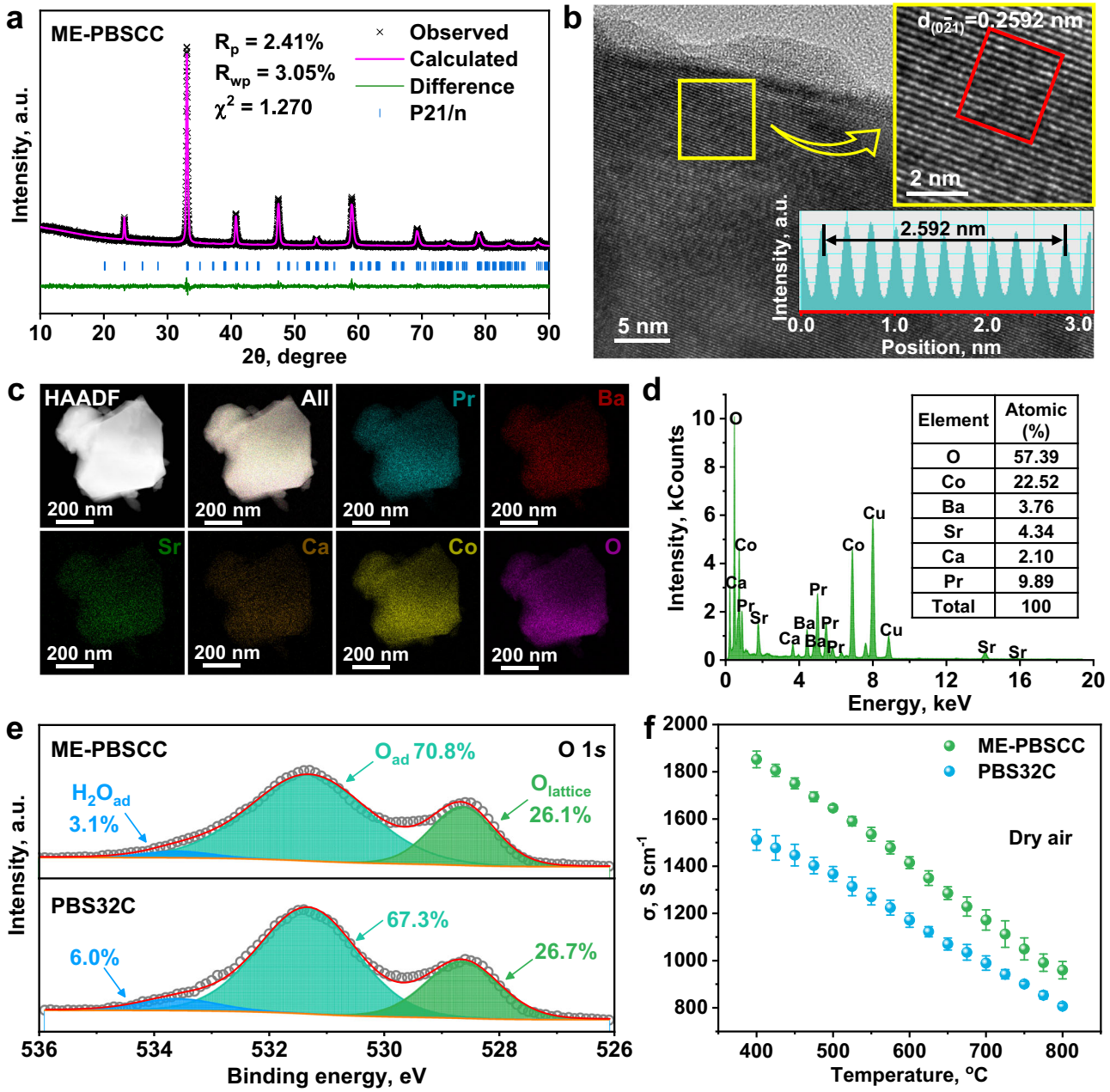

Fig. 1 | Structural and physicochemical characterizations of the ME-PBSCC sample. a XRD patterns of ME-PBSCC with the Rietveld refinement results. **b** HR-TEM images of the ME-PBSCC and a line scanning result along the red frame. **c** HAADF and elemental mapping images of the ME-PBSCC at a scale bar of 200 nm. **d** EDX spectrum and atomic percentage derived from the particle in (**c**). **e** The O 1*s* spectra and **f** the electrical conductivities of ME-PBSCC and PBS32C samples. Each test was conducted in triplicate to obtain statistical standard deviations, presented as error bars.

n) without any impurity phases. The refined lattice parameters of the ME-PBSCC were compiled in Supplementary Table 1. Furthermore, the HR-TEM images of the ME-PBSCC sample after being calcined at 1000 °C for 5 h revealed the strong diffraction planes with a d-spacing distance of 0.2592 nm, likely corresponding to the ME-PBSCC (0$\bar{2}$1) plane (Fig. 1b). Figure 1c presents the high-angle annular dark-field (HAADF) image and elemental mapping images, demonstrating a uniform distribution of all constituent elements in the ME-PBSCC material at the nanoscale without any agglomeration. The atomic percentage of each element obtained from the EDX spectrum was close to the designed stoichiometric ratio (Fig. 1d). The difference between the stoichiometric ratios and the expected values mainly results from the limitations of the EDX instrument and the inhomogeneity of the powder samples. Given the limited resolution of EDX, we additionally performed inductively coupled plasma optical emission spectroscopy (ICP-OES) analysis (Supplementary Fig. 1), which confirmed that all elements were successfully incorporated into ME-PBSCC at compositions essentially matching the nominal values. The content of potential impurities in the as-synthesized ME-PBSCC powder was also evaluated. It is indicated that extremely small amounts of Al and Si were detected (Supplementary Table 2). Moreover, the ME-PBSCC exhibited excellent chemical compatibility with widely used electrolyte materials (including $Gd_{0.1}Ce_{0.9}O_{2-\delta}$ (GDC) and $La_{0.8}Sr_{0.2}Ga_{0.8}Mg_{0.2}O_{3-\delta}$ (LSGM)), as they retained their respective phase structures after co-firing at 1000 °C in air for 2 h (Supplementary Fig. 2).

To reveal how the medium-entropy structure enhances the catalytic performance for ORR and OER at the oxygen electrode, we further

investigated the intrinsic oxygen properties, electrical conductivity, and the chemical state of the B-site transition metal of the samples. The surface structural property of the ME-PBSCC and $Pr_{0.5}Ba_{0.3}Sr_{0.2}CoO_{3-\delta}$ (PBS32C, S_{config} = 1.030R, served as the control) was first evaluated with X-ray photoelectron spectroscopy (XPS) analysis. The ORR and OER activities of the functional oxygen electrodes are closely related to the level of weakly bound oxygen species on the material surface[52]. Figure 1e presents the O 1*s* spectra and the corresponding deconvolution components, which can be assigned to lattice oxygen species ($O_{lattice}$), weakly bound adsorbed oxygen species (O_{ad}), and adsorbed molecular water (H_2O_{ad}) in order of increasing binding energy. It is reported that the oxygen activation capability of oxygen electrodes can be indicated by the values of $O_{ad}/O_{lattice}$[53,54]. The ME-PBSCC demonstrated a higher value of 2.71 for $O_{ad}/O_{lattice}$ than 2.52 in the PBS32C, implying the generation of a higher concentration of extra surface oxygen vacancies on the ME-PBSCC at room temperature. Shown in Supplementary Fig. 3 are the deconvoluted results of Co $2p_{3/2}$ and Ba $3d_{5/2}$ spectra. To maintain electrical neutrality, the ME-PBSCC manifested a lower surface average Co oxidation state. Furthermore, the oxygen vacancy concentrations of ME-PBSCC and PBS32C samples at elevated temperatures were determined by iodometric titration, together with the thermogravimetric (TG) analysis. The oxygen non-stoichiometries (δ) of ME-PBSCC and PBS32C at room temperature were determined to be 0.114 and 0.144, respectively (Supplementary Fig. 4). The electron paramagnetic resonance (EPR) spectra and quantitative data of ME-PBSCC and PBS32C at room temperature are presented in Supplementary Fig. 5 and Supplementary Table 3, respectively. It is demonstrated that PBS32C exhibited a slightly higher oxygen vacancy concentration than ME-PBSCC at room temperature, consistent with the results acquired from the iodometric titration method. Before conducting the TG testing, the samples underwent thorough drying at 140 °C to reduce the impact of adsorbed species. Displayed in Supplementary Fig. 6 are the obtained TG curves and the calculated δ values. It is shown that the amount of bulk oxygen vacancy in PBS32C was higher than that in ME-PBSCC. In addition, the electrical conductivities of the samples between 400–800 °C in dry air were evaluated by a four-probe DC method. As depicted in Fig. 1f, the electrical conductivities of ME-PBSCC and PBS32C were 1172.16 ± 43.13 and 989.72 ± 30.26 S cm^{-1} at 700 °C, respectively. It is generally accepted that electronic conduction within the perovskite oxides occurs via electronic hopping along the B-O-B network[55]. The higher electrical conductivity of ME-PBSCC may suggest the formation of more Co-O-Co percolation networks and relatively lower oxygen vacancy concentrations at elevated temperatures, which is consistent with the TG analysis. Moreover, the oxygen transport capability was investigated by the electrical conductivity relaxation (ECR) method, where the transient response to a sudden change in oxygen partial pressure (p_{O2}) from 0.21 to 0.1 atm was recorded. The fitted coefficients of surface oxygen exchange (k_{chem}) and bulk diffusion (D_{chem}) from the response profile at 650–800 °C are exhibited in Supplementary Fig. 7. Markedly, at each temperature, both k_{chem} and D_{chem} of ME-PBSCC demonstrated higher values compared to PBS32C. Overall, these properties of higher surface oxygen vacancy concentration, electrical conductivity, and rapid oxygen exchange and diffusion kinetics strongly indicate that the ME-PBSCC has great potential for superior ORR and OER catalytic activities, as confirmed by the electrochemical evaluation results in the next sections.

Electrocatalytic performance of ME-PBSCC in the absence/presence of Cr contamination

The oxygen electrocatalytic activities and stabilities of the ME-PBSCC electrode in different atmospheres were investigated by electrochemical impedance spectroscopy (EIS) in the LSGM-based symmetrical cells under open-circuit voltage (OCV) conditions. Similarly, the PBS32C and $Pr_{0.5}Ba_{0.2}Sr_{0.3}CoO_{3-\delta}$ (PBS23C, S_{config} = 1.030R) electrodes, which contain the same amount of alkaline-earth metal elements, were used as a comparison. As shown in Fig. 2a and Supplementary Figs. 8–10, among these electrodes, the ME-PBSCC exhibited the lowest area-specific resistances (ASRs) at 600–800 °C in air, suggesting a higher catalytic activity of ME-PBSCC, as confirmed by the measurements of electrical conductivity and ECR. Particularly, the ASRs of the ME-PBSCC oxygen electrode were only 0.010, 0.013, 0.022, 0.049, and 0.125 Ω cm^2 in air at 800–600 °C, respectively, which outperformed the previously reported Co-based oxygen electrodes containing Pr, Ba, and/or Sr[8,11,14,56–59] (Fig. 2a and Supplementary Table 4). Notably, although PBS23C demonstrated a similar electrical conductivity to that of PBS32C (Supplementary Fig. 11), the relatively worse performance of PBS23C could be ascribed to its slower oxygen exchange and diffusion kinetics (Supplementary Fig. 7). To explore the kinetics of oxygen reactions on the ME-PBSCC electrode, the EIS plots of symmetrical cells with ME-PBSCC oxygen electrode were measured at different p_{O2} and 700 °C (Fig. 2b). As the p_{O2} increased, the polarization resistance (R_p) showed a significant decrease. Furthermore, the distribution of relaxation time (DRT) was employed to deconvolute the overall electrode reactions into individual elementary steps. As displayed in Fig. 2c, each corresponding plot could be separated into several distinct processes, represented as low-frequency (LF), intermediate-frequency (IF), and high-frequency (HF) processes, which manifested different sensitivities to the changes in p_{O2}. The reaction orders *n* for each elementary process at different p_{O2} were calculated based on the relationship: $R_p = k(p_{O2})^{-n}$ (Fig. 2d, Supplementary Table 5). Specifically, almost p_{O2}-independent HF process is likely related to O^{2-} transfer across the interfaces between oxygen electrode and electrolyte[60]; the IF process (n = 0.457) may correspond to the adsorption/dissociation of oxygen molecule[61,62]; while the LF process (n = 1.467) exhibited a significant dependence on p_{O2}, indicating that the LF process may be connected with mass transfer of molecular oxygen[27] (Supplementary Note 1, Supplementary Fig. 12). Moreover, we also conducted an identical p_{O2}-dependent test on the symmetrical cells with PBS32C electrode at 700 °C and observed similar behavior (Supplementary Fig. 13).

The electrocatalytic performance of the ME-PBSCC exposed to Cr-containing conditions (3% H_2O humidified air with Crofer 22 APU foils) was also evaluated. Considering the relatively poor electrocatalytic performance of the PBS23C, only the PBS32C was used as a comparison in the subsequent experiments. Before the EIS tests, the symmetrical cells were all maintained at the target temperatures for 0.5 h to ensure a stable ambient atmosphere. As shown in Fig. 2e and Supplementary Figs. 14 and 15, the introduction of Cr contamination inevitably led to the deterioration of the electrocatalytic activity of ME-PBSCC and PBS32C, as suggested by the increased ASRs at all test temperatures. The deteriorated catalytic activity may be caused by the decrease in p_{O2} and the deposition of inert chromates. It should be noted that ME-PBSCC still exhibited lower ASRs than PBS32C. For example, when Cr contamination was introduced, the R_p values of the ME-PBSCC increased from 0.022 to 0.030 Ω cm^2, while the R_p values of PBS32C increased from 0.032 to 0.046 Ω cm^2 at 700 °C (Fig. 2f, g, Supplementary Table 6). Insightfully, the increased R_p under the Cr contamination mainly comes from the IF and LF processes (Fig. 2h, i). It is indicated that the adsorption/dissociation and mass transfer processes of oxygen molecules on the electrodes might be sensitive to Cr contamination. The intensified LF processes in both electrodes under the Cr-contaminated atmosphere may be ascribed to the continuous deposition of Cr species during the prolonged thermal start-up and to the decreased oxygen partial pressure caused by the introduction of gaseous Cr contamination. More importantly, the ME-PBSCC showed superior electrocatalytic stability and remarkable Cr tolerance, as demonstrated in the ASR stability tests at 700 °C (Fig. 2j). Specifically, the degradation rates of the ASRs for ME-PBSCC were 2.10×10^{-4} (cell #1) and

https://doi.org/10.1038/s41467-026-69338-8

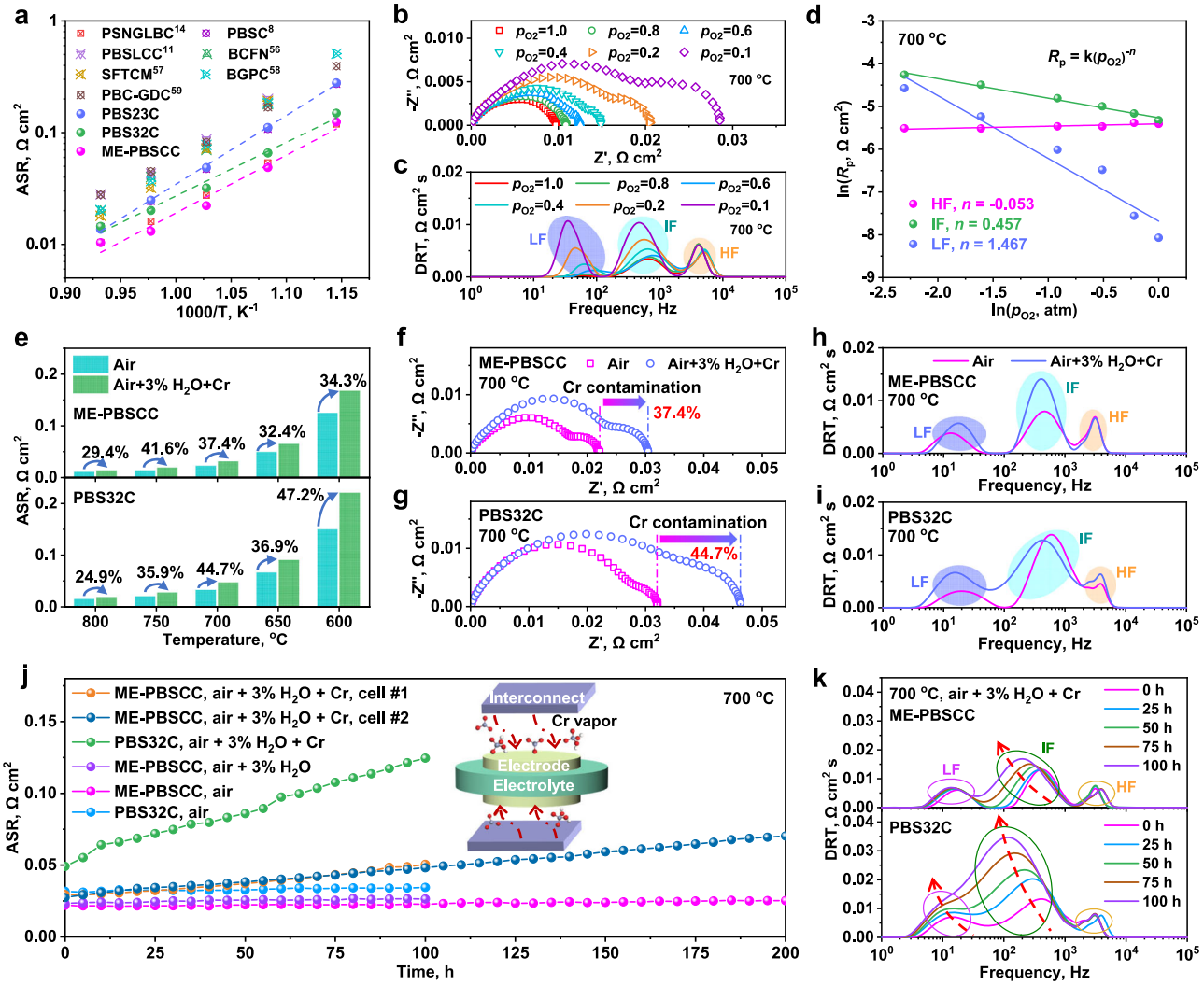

Fig. 2 | Electrocatalytic performance of ME-PBSCC in the absence/presence of Cr contamination. **a** Temperature dependence of ASRs of LSGM-based symmetrical cells with ME-PBSCC, PBS32C, PBS23C, and other previously reported oxygen electrodes (Supplementary Table 4). **b** EIS plots and **c** corresponding DRT plots of ME-PBSCC under various p_{O2} at 700 °C. **d** p_{O2} dependence of each R_p of the elementary processes at 700 °C. **e** Comparison of the ASRs of ME-PBSCC and PBS32C at 600–800 °C in air and in the presence of Cr contamination (air+3% H_2O + Cr). **f**, **g** EIS curves and **h**, **i** corresponding DRT plots of ME-PBSCC and PBS32C before and after the introduction of Cr contaminants at 700 °C. **j** ASRs of ME-PBSCC and PBS32C at 700 °C, as a function of time, measured in air, air+3% H_2O + Cr, and air+3% H_2O, respectively. Cell #1 and cell #2 were tested under identical Cr-contaminated atmosphere for 100 and 200 h, respectively. The inset is the schematic of the symmetrical cell poisoned by gaseous Cr species. **k** Testing time evolution of the DRT plots of ME-PBSCC and PBS32C in wet air with Cr contamination.

2.14×10^{-4} Ω cm^2 h^{-1} (cell #2), respectively, both of which were lower than that of PBS32C (7.55×10^{-4} Ω cm^2 h^{-1}) and comparable to the previously reported Cr-tolerant PSNGLBC (2.60×10^{-4} Ω cm^2 h^{-1})[14]. Figure 2j also indicates that the presence of 3% H_2O did not significantly impair the stability of the ME-PBSCC electrode. To explore the degradation process more deeply, the EIS curves of ME-PBSCC and PBS32C over time in the presence of Cr contamination were further analyzed by DRT (Supplementary Fig. 16). As depicted in Fig. 2k and Supplementary Table 7, the increased ASRs of the ME-PBSCC electrode under the Cr contamination were mainly derived from the resistance of the IF process. However, the PBS32C electrode exhibited a more pronounced rise in the resistances connected with IF and LF processes. The increased IF resistance might be due to the deposited Cr species gradually occupying the active sites for oxygen adsorption and dissociation, while the increase in LF resistance might be caused by the continuous accumulation and agglomeration of Cr species on the surface, preventing effective gas diffusion. As a result, even under Cr-contaminated conditions, ME-PBSCC still exhibited robust electrocatalytic activity and durability.

Performance of Re-SOCs with the ME-PBSCC oxygen electrode in the absence/presence of Cr contamination

To verify the superior electrocatalytic performance of the ME-PBSCC for ORR and OER on realistic single cells, the Re-SOCs with the configuration of Ni-$Zr_{0.84}Y_{0.16}O_{2-\delta}$ (YSZ)|YSZ|GDC|oxygen electrodes were fabricated and evaluated. Figure 3a presents a representative cross-sectional image of the Re-SOC with the ME-PBSCC oxygen electrode. The thicknesses of the YSZ electrolyte and the GDC buffer layer were ~10 and ~2 μm, respectively. The porous ME-PBSCC oxygen electrode was firmly attached to the GDC layer without obvious cracking or delamination. The ME-PBSCC and PBS32C electrodes exhibited similar initial microstructure (Supplementary Fig. 17). Additionally, the Brunauer-Emmett-Teller specific surface areas of as-synthesized ME-PBSCC and PBS32C powders, derived from Nitrogen adsorption/desorption isotherms (Supplementary Fig. 18), were 2.6406 and 3.7060 m^2/g, respectively. As shown in Fig. 3b and Supplementary Fig. 19, the Re-SOCs were first evaluated in the FC mode using wet H_2 (3% H_2O) as fuel and ambient air as oxidant. The single cell with ME-PBSCC oxygen electrode demonstrated remarkable P_{max} of ~2.239,

https://doi.org/10.1038/s41467-026-69338-8

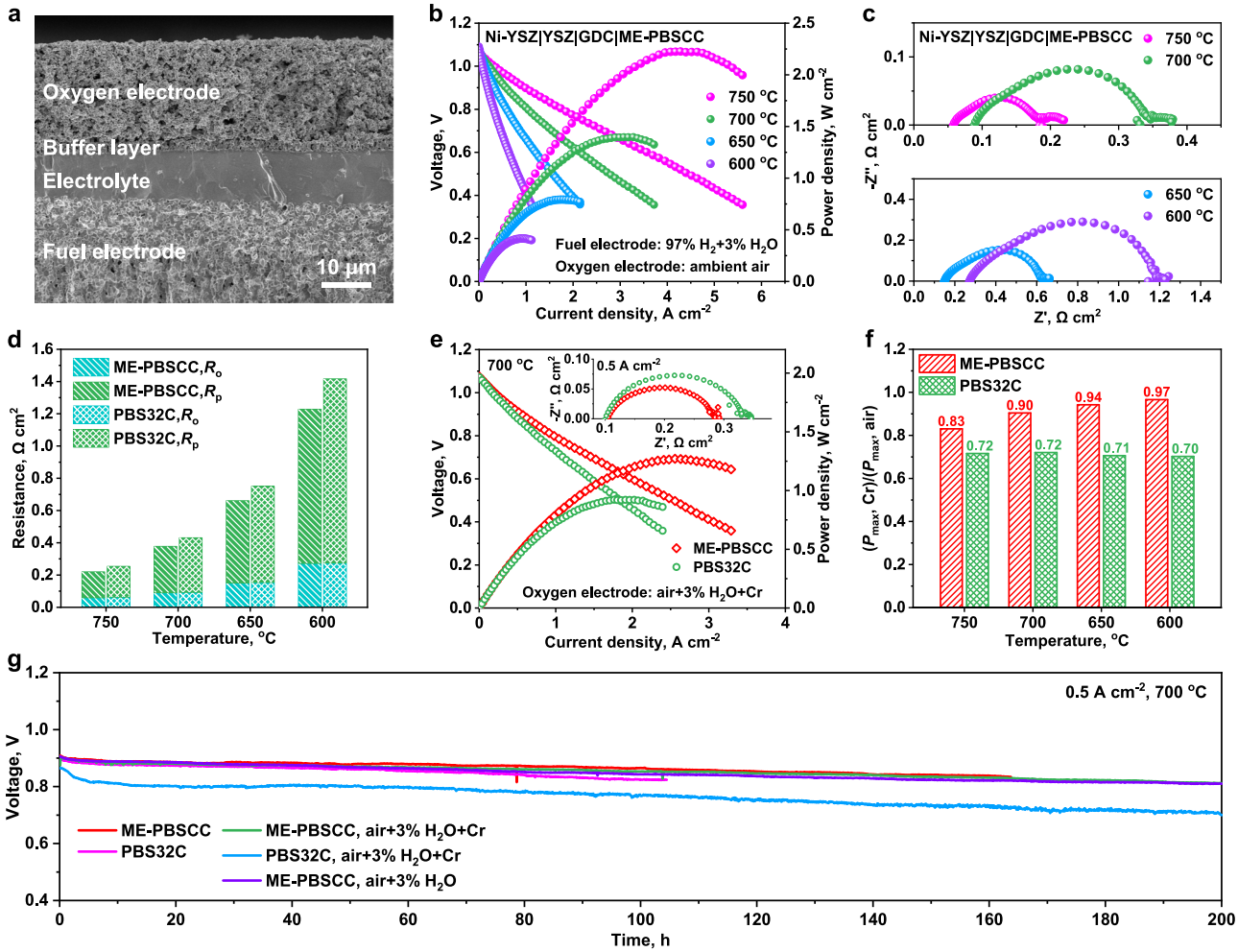

Fig. 3 | Performance of Re-SOCs with the ME-PBSCC oxygen electrode in FC mode in the absence/presence of Cr contamination. a Cross-sectional image of the Re-SOC with ME-PBSCC oxygen electrode after electrochemical evaluation. **b** Typical *I*–*V*–*P* curves of the single cell with ME-PBSCC oxygen electrode in FC mode using wet H_2 and ambient air. **c** EIS curves of the single cell with ME-PBSCC oxygen electrode at 750–600 °C. **d** R_o and R_p of the single cells with ME-PBSCC and PBS32C oxygen electrodes. **e** The *I*–*V*–*P* curves and corresponding EIS at 0.5 A cm^{-2} (inset) of the single cells with ME-PBSCC and PBS32C at 700 °C under Cr-containing conditions. **f** The ratios of attenuated P_{max} after the introduction of Cr contamination. **g** Durability of the cells operated at 0.5 A cm^{-2} and 700 °C when the ME-PBSCC and PBS32C oxygen electrodes were exposed to ambient air, air+3% H_2O + Cr, and air+3% H_2O, respectively.

1.405, 0.795, and 0.416 W cm^{-2} at 750, 700, 650, and 600 °C, respectively, superior to the cell with PBS32C oxygen electrode (e.g., 1.287 W cm^{-2} at 700 °C). Significantly, the improved cell performance is mainly due to the smaller R_p values of ME-PBSCC (Fig. 3c, d, and Supplementary Fig. 20), indicating the superior electrocatalytic ORR activity of ME-PBSCC in ambient air (Supplementary Fig. 21 and Supplementary Note 2). When the oxygen electrodes were exposed to a Cr-containing atmosphere (air+3% H_2O + Cr), the single cells with PBSCC and PBS32C experienced different degrees of decline in P_{max} (Supplementary Figs. 22a, b and 23). Notably, under Cr contamination, the ohmic resistance (R_o) values of the single cells remained almost constant, and the increased R_p values dominated the degradation in cell performance at 600–750 °C (Supplementary Fig. 22c, d), which may be caused by the decrease in the surrounding p_{O2} and the poisoning of Cr vapor. Nevertheless, even under this Cr-contaminated atmosphere, ME-PBSCC still exhibited faster kinetics of ORR (Supplementary Fig. 24 and Supplementary Note 2). For instance, the P_{max} of single cells with ME-PBSCC and PBS32C were determined to be 1.271 and 0.927 W cm^{-2} at 700 °C in the presence of Cr contamination (Fig. 3e). Even at a constant current of 0.5 A cm^{-2}, the ME-PBSCC still exhibited a lower R_p value, as shown in the inset in Fig. 3e. Furthermore, after the introduction of Cr species, the ratios of attenuated P_{max} could be an important factor in evaluating the Cr tolerance of oxygen electrodes (denoted as $(P_{max,\ Cr})/(P_{max,\ air})$). As shown in Fig. 3f, the ME-PBSCC exhibited larger ratios of $(P_{max,\ Cr})/(P_{max,\ air})$ than those of the PBS32C, especially at reduced temperatures, implying the excellent Cr-poisoning resistance of the ME-PBSCC. More importantly, even in a Cr-containing atmosphere, the performance of our cell utilized ME-PBSCC oxygen electrode surpassed that of most state-of-the-art oxygen electrode materials reported in the air (Supplementary Table 8)[14,63–72]. Shown in Fig. 3g are the stabilities of Re-SOCs with ME-PBSCC and PBS32C oxygen electrodes in FC mode at 0.5 A cm^{-2} and 700 °C. The cells with the ME-PBSCC exhibited better operational stability than those of the PBS32C, regardless of whether the oxygen electrodes were exposed to ambient air or a Cr-containing atmosphere. In particular, the degradation rates of ME-PBSCC and PBS32C in the Cr-contaminated atmosphere were around 4.31×10^{-4} and 8.17×10^{-4} V h^{-1} at 700 °C, respectively. It is worth noting that the rapid degradation observed in the first 5 h for the cell with PBS32C oxygen electrode could be attributed to the rapid decline in oxygen exchange capability and electrical conductivity of PBS32C in the initial stage caused by Cr poisoning (see the next section). Additionally, exposure to water alone was evaluated in the single-cell tests (Fig. 3g). The results suggested that 3% H_2O did not noticeably affect the stability of

the cell, in agreement with the results obtained from the symmetrical cell with ME-PBSCC electrode in 3% H_2O humidified air. Post-mortem microstructural investigations of the cells after durability tests at 700 °C were conducted by SEM. As shown in Supplementary Fig. 25, a much rougher surface was observed on the PBS32C oxygen electrode, which might be responsible for its marginally accelerated degradation in air. Supplementary Fig. 26 displays a comprehensive morphological comparison of the cells with ME-PBSCC and PBS32C oxygen electrodes after stability tests in FC mode under Cr-contaminated air. Good adhesion between the layers of the cells was maintained after the test (Supplementary Fig. 26a, b). And the volatile Cr species were mainly deposited on the surface of the oxygen electrodes. Compared with PBS32C, the relatively small amount of Cr deposition may be attributed to the entropy-dominated structural stability of ME-PBSCC, which inhibited the surface segregation of nucleating agents such as Ba^{2+} and Sr^{2+}. The EDX mapping was used to further determine the composition of surface species (Supplementary Figs. 27–29). Interestingly, it is indicated that the deposits on the surface of the two oxygen electrodes after durability tests are mainly $BaCrO_4$ rather than $SrCrO_4$, which may be attributed to the fact that the formation of the $BaCrO_4$ phase exhibits a more negative Gibbs free energy thermodynamically (Supplementary Fig. 30). It also reminds us that, despite the well-documented detriments of Sr segregation[73–75], the adverse effects of Ba segregation should not be overlooked in materials containing both Ba and Sr, especially under a Cr-contaminated atmosphere.

The electrocatalytic activity and stability of ME-PBSCC for OER in the presence of Cr contamination were also investigated. Figure 4a shows the electrolysis performance of Re-SOCs with the ME-PBSCC at 700 °C when the oxygen electrode was exposed to Cr contamination and the fuel electrode operated at different water vapor contents. Impressive electrolysis current densities of −1.10, −0.96, and −0.80 A cm^{-2} at 700 °C and 1.3 V were attained at 50, 40, and 30% water contents, respectively. When the water content increased, the increase in current densities was attributed to the decrease in R_p, as shown in Fig. 4b, Supplementary Figs. 31 and 32, and Supplementary Note 2. The fitting values of these EIS curves were summarized in Supplementary Table 9. The current density obtained for 50% H_2O electrolysis at 1.3 V and 700 °C under Cr-containing conditions remains competitive with numerous previously reported results based on similar cell configurations in Cr-free atmosphere (Supplementary Table 10)[8,12,76–81]. The electrolysis performance at higher water contents (e.g., 70% and 90%) was also evaluated (Supplementary Fig. 33). At 700 °C and 1.3 V, the Re-SOC with ME-PBSCC oxygen electrode achieved excellent current densities of −1.48 and −1.29 A cm^{-2} at water contents of 90% and 70%, respectively. Furthermore, as shown in Fig. 4c, the relatively stable voltages were delivered by continuously electrolyzing 30% H_2O at −0.5 A cm^{-2} and 700 °C in a Cr-containing atmosphere. More importantly, a good reversible operation capability of Re-SOCs should also be highlighted (Fig. 4d). The Re-SOC with the developed ME-PBSCC oxygen electrode demonstrated a promising reversible operation stability for 100 h (25 cycles) at 700 °C, which is the first reported Re-SOC operating in reversible mode under Cr-contaminated conditions. These results strongly confirmed that the ME-PBSCC has the potential to realize efficient and stable electrocatalytic capabilities for ORR and OER under realistic operating conditions. Shown in Supplementary Fig. 34 are the cross-sectional and surface SEM images of the cells with ME-PBSCC oxygen electrodes after durability tests in EC and reversible modes under Cr-contaminated air. The volatile Cr species also deposited on the surface of the oxygen electrodes in both EC and reversible modes, showing the same Cr deposition behavior as that in FC mode. Furthermore, EDX mapping demonstrated that these deposited Cr species remain predominantly in the $BaCrO_4$ phase (Supplementary Figs. 35 and 36).

Characterization and analysis of enhanced Cr tolerance of ME-PBSCC

To verify the chemical reactivities of ME-PBSCC and PBS32C with Cr_2O_3, powder samples of each material were mixed with Cr_2O_3 and

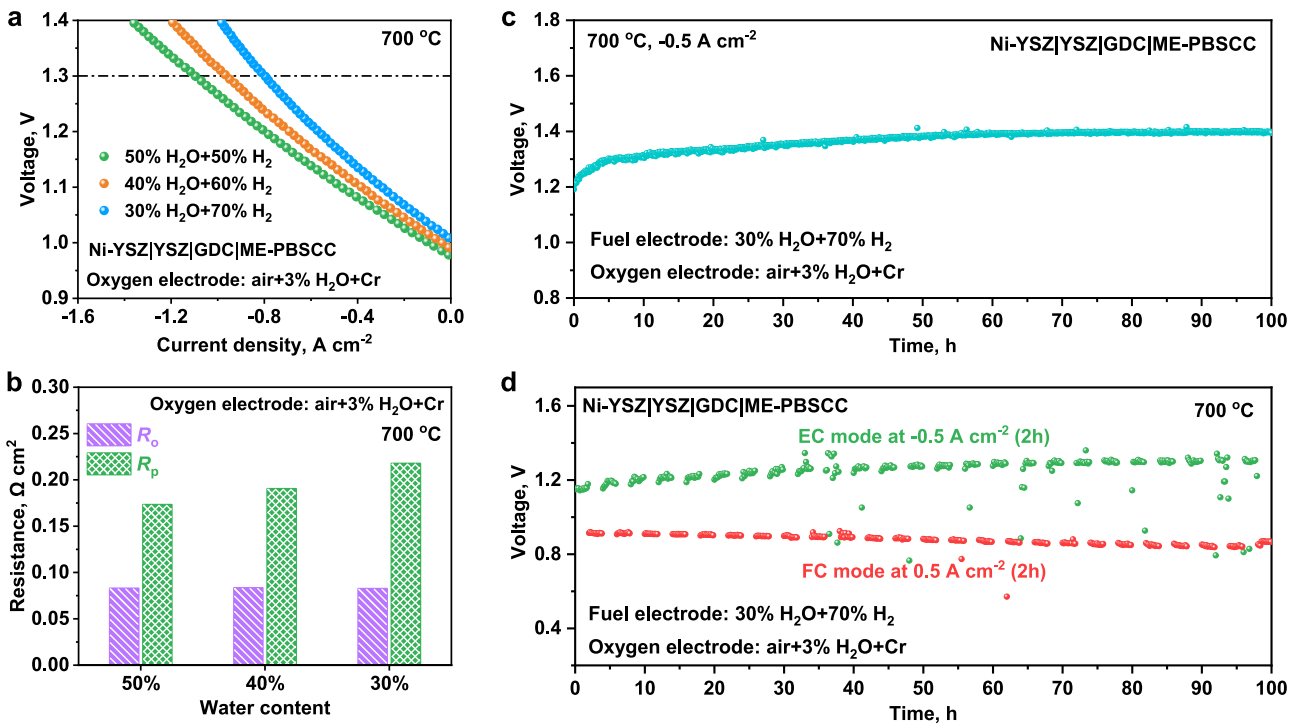

Fig. 4 | Performance of Re-SOCs with the ME-PBSCC oxygen electrode in EC mode in the presence of Cr contamination. a Typical *I*–*V* curves and **b** corresponding resistances (R_o and R_p) of the single cell with ME-PBSCC oxygen electrode in EC mode at 700 °C when the oxygen electrode was exposed to Cr contamination. Durability of the Re-SOCs with ME-PBSCC oxygen electrode operated in **c** EC mode (−0.5 A cm^{-2}) and **d** reversible mode (±0.5 A cm^{-2}) at 700 °C when the fuel electrodes were fueled with 30% H_2O humidified H_2 and the oxygen electrodes were exposed to Cr contamination.

then subjected to heat treatment at 700 °C for 100 h in air. As marked in Fig. 5a, the $BaCrO_4$ phase was detected in the mixture of PBS32C and Cr_2O_3 powders. However, it was not detected in the mixtures of ME-PBSCC and Cr_2O_3 treated in either air or 3% H_2O humidified air, presumably because their concentrations fall below the detection threshold of XRD. It is suggested that ME-PBSCC has better structural stability against the Cr contamination. Furthermore, the surface properties were investigated to gain a deeper understanding of the enhanced Cr tolerance of ME-PBSCC. Displayed in Fig. 5b are the stabilities of k_{chem} values of ME-PBSCC and PBS32C in the absence and presence of Cr_2O_3 at 700 °C for 100 h, respectively. The k_{chem} values of both ME-PBSCC and PBS32C samples exhibited significant attenuation in a Cr-containing atmosphere. As shown in Supplementary Fig. 37, the initial values measured without Cr_2O_3 were used as the k_{chem} values at 0 h. After being exposed to Cr contamination for 1 h (to stabilize the atmosphere of the test system), the k_{chem} values of ME-PBSCC and PBS32C were determined to be 6.052×10^{-4} and 3.613×10^{-4} cm s^{-1}, respectively. When exposed to Cr contamination for 100 h, the k_{chem} value of ME-PBSCC was 1.766×10^{-4} cm s^{-1}, significantly higher than that of PBS32C (0.394×10^{-4} cm s^{-1}). Shown in Supplementary Fig. 38 are the electrical conductivities as a function of time at 700 °C in the presence of Cr contamination. It is also indicated that PBS32C exhibited a more rapid decline in electrical conductivity than ME-PBSCC over 100 h in a Cr-containing atmosphere. In addition, Raman spectroscopy was utilized to analyze the accumulation and distribution of Cr deposits on the surface of oxygen electrodes after stability tests. Regardless of the operating modes, significantly weaker vibrational peaks of Cr_2O_3 and CrO_4^{2-} were detected on the ME-PBSCC surface after stability tests (Fig. 5c). Unlike the widely reported Cr deposition behaviors of $La_{1-x}Sr_xMnO_{3-\delta}$[17,82–84], no chromate-related signal was observed on the surface of the GDC layers after oxygen electrode stripping in all operating modes (Supplementary Fig. 39), which further confirmed that the deposition of Cr species only occurred on the oxygen electrode surface in this work. The only observed vibrational peaks in the Raman spectra could belong to the feature of the GDC. Raman mappings of Cr_2O_3 and CrO_4^{2-} were performed to further reveal the accumulation of Cr deposits on the surface of ME-PBSCC and PBS32C oxygen electrodes after stability tests in FC mode. As depicted in Fig. 5d, e, compared with the PBS32C, significantly lower signals of Cr_2O_3 and CrO_4^{2-} were detected on the ME-PBSCC after stability tests. In addition, it is reported that the existence of polarization current affected the distribution and accumulation of Cr deposits[51,82,85,86]. To eliminate the influence of polarization current, porous ME-PBSCC and PBS32C pellet samples (with the same calcination temperature and time as the oxygen electrode) were fabricated to evaluate the Cr-poisoning behaviors of the materials (Supplementary Fig. 40a). Similarly, Raman analysis revealed more severe poisoning phenomena on the PBS32C sample after being annealed at 700 °C for 200 h in the Cr-containing atmosphere (Supplementary Fig. 40b). We also investigated the cleaved surface of the porous pellet samples after treatment (Fig. 5f–h). Notably, deeper Cr diffusion was detected in the PBS32C sample compared to ME-PBSCC (Fig. 5i, j). It may significantly affect the oxygen surface exchange and gas diffusion of the materials, which is consistent with the analytical results of EIS data based on symmetrical cells. The dense pellets of ME-PBSCC and PBS32C using a traditional sintering process were also fabricated and subjected to Cr treatment under identical conditions. The Raman results of the surface of dense samples after being annealed in the Cr-containing atmosphere are similar to those of the porous samples (Supplementary Figs. 41 and 42). Notably, no Cr-related feature was detected on the cleaved surfaces adjacent to the Cr-exposed side of the dense pellets (Supplementary Fig. 43), which further confirmed that Cr species migrated to and deposited on the electrode through gas-phase diffusion, without directly corroding or disrupting the near-surface perovskite structure in the depth direction. In general, these outcomes demonstrate the superior structural stability and outstanding Cr-poisoning tolerance of ME-PBSCC, which are consistent with the results of electrochemical evaluations.

Discussion

In summary, we developed a medium-entropy PBSCC perovskite material as an oxygen electrode for Re-SOC applications, demonstrating highly competitive electrochemical performance and Cr tolerance. The abundant surface oxygen vacancy concentration, high electrical conductivity, and rapid oxygen exchange and diffusion kinetics of the ME-PBSCC oxygen electrode ensured the excellent ORR and OER activities, as confirmed by the physicochemical characterizations and electrochemical evaluation. Furthermore, the impressive Cr tolerance of Re-SOCs with ME-PBSCC was demonstrated in multiple operating modes. The properties of the poisoned surface of materials under different test conditions were systematically analyzed by tools such as ECR and Raman spectroscopy. More importantly, the developed ME-PBSCC oxygen electrode has achieved the highly promising stable operation of Re-SOCs in FC, EC, and reversible modes in the presence of Cr contamination. This study may provide an effective strategy for the rational design of active, durable, and contaminant-tolerant oxygen electrodes for high-performance Re-SOCs and other energy storage and conversion devices.

Methods

Chemicals

$PrN_3O_9{\cdot}6H_2O$ (99%), $Co(NO_3)_2{\cdot}6H_2O$ (99%), ethylenediaminetetraacetic acid (EDTA, 99.5%), La_2O_3 (99%), $SrCO_3$ (99%), Ga_2O_3 (99.8%), MgO (99.9%), triethanolamine (≥ 99%), Polyvinyl butyral (PVB), Polyvinylpyrrolidone (PVP), and ethyl cellulose were all purchased from Shanghai Macklin Biochemical Co., Ltd. BaN_2O_6 (99.5%), N_2O_6Sr (99.5%), and N-Methyl pyrrolidone (NMP, ≥99%) were purchased from Shanghai Aladdin Biochemical Co., Ltd. $Ca(NO_3)_2{\cdot}4H_2O$ (≥99%) and acetone (≥99.5%) were purchased from Guangzhou Chemical Reagent Factory. Citric acid (CA) was purchased from Sinopharm Chemical Reagent Co., Ltd. Ammonia solution (NH_4OH, 25%-28%) was supplied by Tianjin Damao Chemical Reagent Factory. Ethanol absolute was purchased from Tianjin Kemao Chemical Reagent Co., Ltd. Terpineol was purchased from Alfa Aesar (China) Chemical Co., Ltd. Silver paste was purchased from Shanghai Synthetic Resin Research Institute. The NiO, YSZ, and GDC powders were all purchased from Zhejiang H2-Bank Technology Co., Ltd.

Preparation of powders

ME-PBSCC, PBS32C, and PBS23C powders were prepared by a sol-gel complexing method. A stoichiometric amount of metal nitrates was mixed with EDTA and CA in deionized water with the molar ratio of metal ions: EDTA: CA = 1: 1: 2. Then, NH_4OH was added to adjust the pH value of the solution to ~7. The gels formed after the evaporation of water were fired at 300 °C for 5 h. Finally, the precursors were further calcined at 1000 °C for 5 h to obtain the final oxygen electrode powders. The LSGM powder was prepared by a solid-state reaction method. La_2O_3 and MgO powders were pre-fired at 1000 °C for 2 h to remove adsorbed moisture. Stochiometric amounts of La_2O_3, $SrCO_3$, Ga_2O_3, and MgO were mixed in absolute ethanol and ball-milled for 24 h. The mixture was thoroughly dried and calcined at 1250 °C for 5 h to obtain raw LSGM powder. All the prepared powders should be stored in a sealed condition.

Fabrication of symmetrical cells

LSGM pellets were prepared by uniaxially pressing the raw LSGM powders, followed by being calcined at 1450 °C for 5 h. The oxygen electrode powders (1 g) were ball-milled at 450 rpm for 2 h and then

https://doi.org/10.1038/s41467-026-69338-8

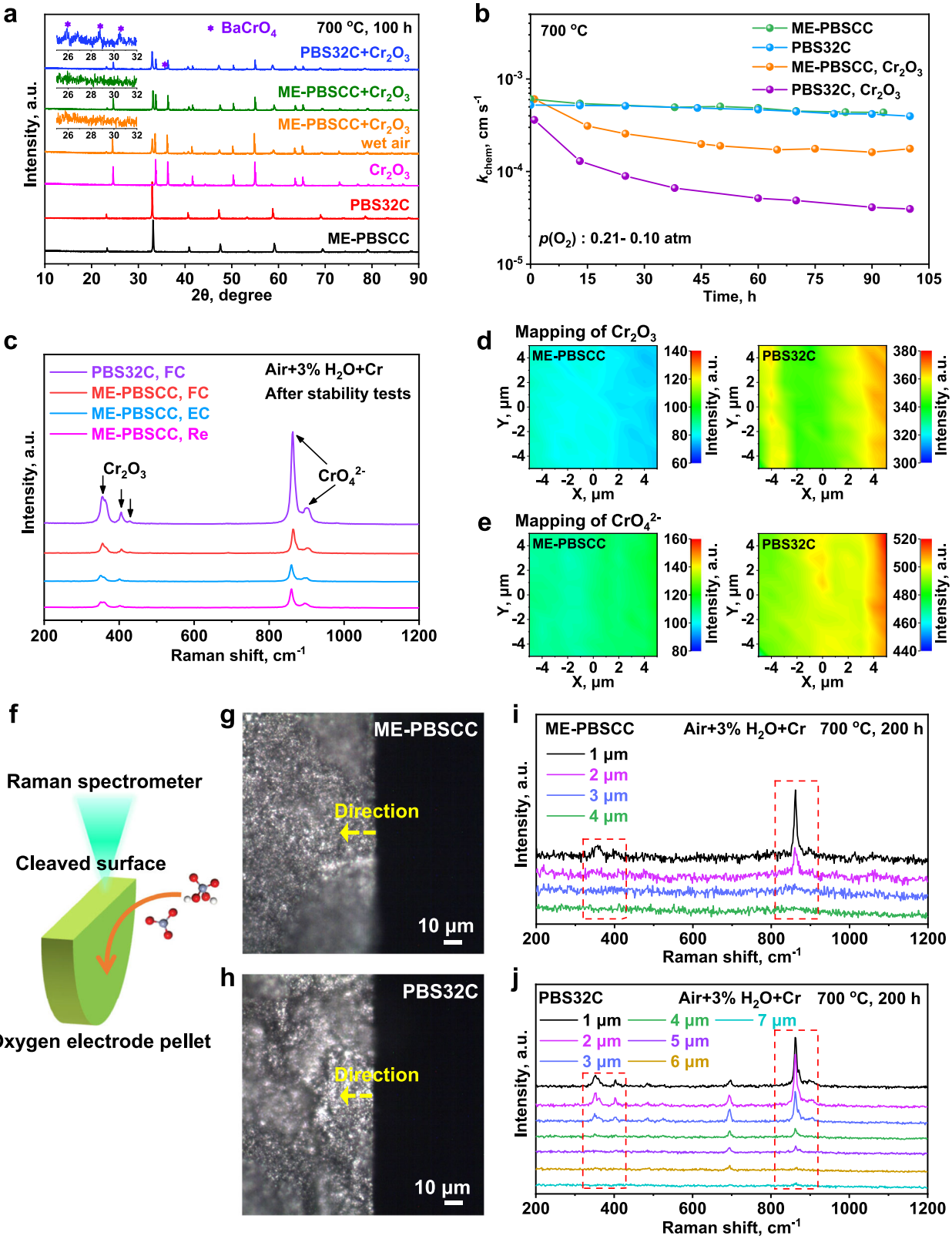

Fig. 5 | Characterization and analysis of enhanced Cr tolerance of ME-PBSCC. **a** The chemical compatibility of ME-PBSCC and PBS32C with Cr_2O_3 after being treated in air and 3% H_2O humidified air at 700 °C for 100 h. **b** The k_{chem} as a function of time at 700 °C in the absence and presence of Cr_2O_3 powder. **c** Raman spectra on the surface of oxygen electrodes after stability tests in different operating modes in the Cr-contaminated air. **d**, **e** Raman mapping of Cr_2O_3 and CrO_4^{2-} on the surface of ME-PBSCC and PBS32C oxygen electrodes after stability tests at 700 °C, respectively. **f** Schematic diagram of Raman analysis on the cleaved surface of a pellet after poisoning by Cr contaminants. **g**, **h** Optical images of the cleaved surfaces of porous ME-PBSCC and PBS32C pellets after being annealed in the Cr-containing atmosphere at 700 °C for 200 h. **i**, **j** Raman spectra along the yellow lines in (**g**, **h**) on the cleaved surfaces.

mixed and ground with terpineol (0.76 g) and ethyl cellulose (0.04 g) to prepare the oxygen electrode slurries. LSGM-based symmetrical cells were prepared by painting the oxygen electrode slurries onto both sides of LSGM pellets. The active area of the single side is 0.2826 cm^2. The cells (with a configuration of oxygen electrode|LSGM|oxygen electrode) were then sintered at 1000 °C for 2 h to form porous oxygen electrodes.

Fabrication of single cells

The configuration of the fuel electrode-supported single cell was NiO-YSZ|YSZ|GDC|oxygen electrode. The NiO-YSZ fuel electrode-supported substrate was prepared via a modified phase inversion method. PVP, polyethersulfone (PESf), and NMP with a weight ratio of 1: 4: 24 were mixed to form an organic solution. The fuel electrode slurry was prepared by mixing NiO (27 g), YSZ (18 g), and organic solution (21.75 g) and then ball milling for 48 h. The graphite layer slurry was prepared by mixing graphite (7 g) and organic solution (18.125 g) for at least 48 h. The obtained graphite layer slurry and fuel electrode slurry were cast onto the smooth glass in sequence, followed by immediately immersing in deionized water for 10 h. Phase inversion took place as mass exchange between the slurries and water. After drying overnight in ambient air, the obtained substrate was punched into pellets. The raw pellets were first pre-fired at 1000 °C for 2 h to remove the organic components and graphite layers and to enhance their mechanical strength. The dispersant was prepared from 1 g PVB, 1 g triethanolamine, and 8 g anhydrous ethanol. To prepare electrolyte/functional layer slurries, 1 g YSZ or 0.5 g YSZ with 0.5 g NiO were separately mixed with 0.5 g dispersant and 10 g anhydrous ethanol and then ball-milled for 24 h. The NiO-YSZ functional layer and the YSZ electrolyte slurries were successively dripped onto the calcined fuel electrode pellets. After drying, these pellets were calcined at 1350 °C for 5 h to form NiO-YSZ fuel electrode-supported half cells. The slurry of the GDC buffer layer was prepared by mixing GDC (0.5 g), acetone (10 g), terpineol (1.9 g), and ethyl cellulose (0.1 g), and ball milling for 24 h. The GDC slurry was dripped onto the half-cell and co-fired at 1300 °C for 2 h in air. Finally, the oxygen electrode slurries were painted onto the surface of the GDC layer (with an active area of 0.196 cm^2) and then sintered at 1000 °C for 2 h. After that, two pieces of Ag mesh, coated with a thin layer of Ag paste, were attached to the fuel electrode and oxygen electrode of single cells and then dried to solidify the Ag paste.

Material characterizations

Phase structures of prepared powders were examined by XRD (Bruker D8 Advance). The microstructure and morphology of the cells were examined using a cold field emission SEM (Hitachi SU8010). The actual atomic ratios of each element in the as-synthesized powders were measured by ICP-OES (Agilent 7700). The TEM (Thermo Talos F200X G2) equipped with an EDX was employed to obtain the high-resolution images and elemental distribution. The XPS (Thermo Scientific K-Alpha) was employed to explore the chemical states of elements on the surface of the samples. The EPR (Bruker EMXplus-6/1) measurement was employed to compare the oxygen vacancy concentrations. The weight changes of the samples from room temperature to 800 °C in air were detected using TGA (Netzsch TG 209 F3). Raman spectroscopy (Renishaw RM1000) was applied with a wavelength of 514 nm. The prepared oxygen electrode powders were mixed with 1% PVB and then pressed into circular pellets and rectangular bars. Afterward, the green pellets and bars were calcined at 1200 °C for 10 h to form dense pellets and bars. The electronic conductivity and ECR were measured using dense rectangular bars. The dense pellets treated with Cr vapor were used for Raman testing.

Electrochemical measurements

The symmetrical cells were tested under OCV conditions at 600–800 °C in air and Cr-containing atmosphere (air+3% H_2O + Cr), respectively. The different oxygen partial pressures were realized by adjusting the flow rates of pure O_2 and pure Ar. The single cell was mounted on an alumina supporting tube by the ceramic adhesive (Aremco 552) for electrochemical tests. The Crofer 22 APU foils with no protective coating were used to create a Cr-containing atmosphere, which was placed about 2 mm away from the oxygen electrodes. The Cr vaporization rates from uncoated Crofer 22 APU were likely in the order of $2.0–6.0 \times 10^{-10}$ kg m^{-2} s^{-1} at 800 °C[87]. The partial pressures of gaseous CrO_3 and $CrO_2(OH)_2$ are approximately 1.0×10^{-10} and 3.0×10^{-7} atm (700 °C, 21% p_{O2}, and 3% p_{H2O}), respectively[31,88]. For the tests in FC mode, the fuel electrode was supplied with 3% H_2O humidified H_2, and the oxygen electrode was exposed to ambient air or the Cr-containing atmosphere. For the tests in EC mode, the fuel electrode was supplied with 50%, 40%, and 30% H_2O humidified H_2, and the oxygen electrode was exposed to the Cr-containing atmosphere. Particularly, for the stability tests in electrolysis and reversible modes, the fuel electrode was fed with 30% H_2O humidified H_2, and the oxygen electrode was exposed to the Cr-containing atmosphere. It is worth noting that, unlike single cells, the Crofer 22 APU foils are placed adjacent to oxygen electrodes as a Cr source on both sides of symmetrical cells. The EIS and *I–V* curves were measured by a multi-channel electrochemical workstation (Parstat MC200, Princeton Applied Research). All voltage was not iR corrected. The frequency range for all EIS curves was measured from 10^5 Hz to 0.1 Hz with an AC amplitude of 10 mV. All electrochemical data were collected and processed using VersaStudio software. Apart from the conductivity test, all other electrochemical tests and comparisons were conducted only once.

Data availability

The data supporting the findings of this study are available within the paper and the Supplementary Information file. Source data are provided with this paper.

References

1. Fankhauser, S. et al. The meaning of net zero and how to get it right. *Nat. Clim. Change* **12**, 15–21 (2022).
2. Fuso et al. Mapping synergies and trade-offs between energy and the Sustainable Development Goals. *Nat. Energy* **3**, 10–15 (2018).
3. Gielen, D. et al. The role of renewable energy in the global energy transformation. *Energy Strategy Rev.* **24**, 38–50 (2019).
4. Duan, C. et al. Highly efficient reversible protonic ceramic electrochemical cells for power generation and fuel production. *Nat. Energy* **4**, 230–240 (2019).
5. Graves, C., Ebbesen, S. D., Jensen, S. H., Simonsen, S. B. & Mogensen, M. B. Eliminating degradation in solid oxide electrochemical cells by reversible operation. *Nat. Mater.* **14**, 239–244 (2014).
6. Ebbesen, S. D., Jensen, S. H., Hauch, A. & Mogensen, M. B. High temperature electrolysis in alkaline cells, solid proton conducting cells, and solid oxide cells. *Chem. Rev.* **114**, 10697–10734 (2014).
7. Kim, J. H. et al. An universal oxygen electrode for reversible solid oxide electrochemical cells at reduced temperatures. *Energy Environ. Sci.* **16**, 3803–3814 (2023).
8. Zhu, F. et al. Entropy and composition regulations of air electrodes enable efficient oxygen reduction and evolution reactions for reversible solid oxide cells. *Adv. Energy Mater.* **14**, 2401048 (2024).
9. Khan, M. S., Xu, X., Knibbe, R. & Zhu, Z. Air electrodes and related degradation mechanisms in solid oxide electrolysis and reversible solid oxide cells. *Renew. Sustain. Energy Rev.* **143**, 110918 (2021).
10. Chen, Y. et al. Advances in cathode materials for solid oxide fuel cells: complex oxides without alkaline earth metal elements. *Adv. Energy Mater.* **5**, 1500537 (2015).
11. He, F. et al. A reversible perovskite air electrode for active and durable oxygen reduction and evolution reactions via the A-site entropy engineering. *Mater. Today* **63**, 89–98 (2023).

12. Li, X. et al. An active and stable high-entropy Ruddlesden-Popper type $La_{1.4}Sr_{0.6}Co_{0.2}Fe_{0.2}Ni_{0.2}Mn_{0.2}Cu_{0.2}O_{4\pm\delta}$ oxygen electrode for reversible solid oxide cells. *Adv. Funct. Mater.* **34**, 2411216 (2024).
13. Tong, X. et al. Promotion of oxygen reduction and evolution by applying a nanoengineered hybrid catalyst on cobalt free electrodes for solid oxide cells. *J. Mater. Chem. A* **8**, 9039–9048 (2020).
14. Zhu, F. et al. An active and contaminants-tolerant high-entropy electrode for ceramic fuel cells. *ACS Energy Lett.* **9**, 556–567 (2024).
15. Schuler, J. A. et al. Air side contamination in Solid Oxide Fuel Cell stack testing. *J. Power Sources* **196**, 7225–7231 (2011).
16. Fergus, J. W. Metallic interconnects for solid oxide fuel cells. *Mater. Sci. Eng.: A* **397**, 271–283 (2005).
17. Jiang, S. P. & Chen, X. Chromium deposition and poisoning of cathodes of solid oxide fuel cells—a review. *Int. J. Hydrog. Energy* **39**, 505–531 (2014).
18. Huang, Y. L., Hussain, A. M., Pellegrinelli, C., Xiong, C. & Wachsman, E. D. Chromium poisoning effects on surface exchange kinetics of $La_{0.6}Sr_{0.4}Co_{0.2}Fe_{0.8}O_{3-\delta}$. *ACS Appl. Mater. Interfaces* **9**, 16660–16668 (2017).
19. Liu, W. & Konysheva, E. Y. Conductivity of $SrCrO_4$ and its influence on deterioration of electrochemical performance of cathodes in solid oxide fuel cells. *ECS Trans.* **59**, 327 (2014).
20. Chen, K., Ai, N., O'Donnell, K. M. & Jiang, S. P. Highly chromium contaminant tolerant BaO infiltrated $La_{0.6}Sr_{0.4}Co_{0.2}Fe_{0.8}O_{3-\delta}$ cathodes for solid oxide fuel cells. *Phys. Chem. Chem. Phys.* **17**, 4870–4874 (2015).
21. Stodolny, M. K., Boukamp, B. A., Blank, D. H. A. & van Berkel, F. P. F. Cr-poisoning of a $LaNi_{0.6}Fe_{0.4}O_3$ cathode under current load. *J. Power Sources* **209**, 120–129 (2012).
22. Hassan, M. A., Mamat, O. B. & Mehdi, M. Review: Influence of alloy addition and spinel coatings on Cr-based metallic interconnects of solid oxide fuel cells. *Int. J. Hydrog. Energy* **45**, 25191–25209 (2020).
23. Zhu, J. H., Chesson, D. A. & Yu, Y. T. Review—$(Mn,Co)_3O_4$-based spinels for SOFC interconnect coating application. *J. Electrochem. Soc.* **168**, 114519 (2021).
24. Zhao, Y. et al. $CuFe_2O_4$ nano-spherical powder directly served as interconnect coating for solid oxide fuel cells applications. *J. Power Sources* **599**, 234221 (2024).
25. Uddin, M. A. et al. Electrochemical validation of in-cell chromium getters to mitigate chromium poisoning in SOFC stack. *J. Electrochem. Soc.* **164**, F1342 (2017).
26. Hong, J. et al. Strontium manganese oxide getter for capturing airborne Cr and S contaminants in high-temperature electrochemical systems. *ACS Appl. Mater. Interfaces* **11**, 34878–34888 (2019).
27. Niu, Y. et al. Enhancing oxygen reduction activity and Cr tolerance of solid oxide fuel cell cathodes by a multiphase catalyst coating. *Adv. Funct. Mater.* **31**, 2100034 (2021).
28. Huang, J. et al. Promotional role of $BaCO_3$ on the chromium–tolerance of $La_{0.6}Sr_{0.4}Co_{0.2}Fe_{0.8}O_{3-\delta}$ cathodes of solid oxide fuel cells. *Appl. Catal. B Environ.* **321**, 122080 (2023).
29. Han, X. et al. A durable and highly active oxygen electrode for solid oxide cells: new insight into segregation suppression of layered perovskite. *Adv. Mater.* **37**, 2502068 (2025).
30. Grolig, J. G., Froitzheim, J. & Svensson, J. E. Coated stainless steel 441 as interconnect material for solid oxide fuel cells: oxidation performance and chromium evaporation. *J. Power Sources* **248**, 1007–1013 (2014).
31. Zhou, L., Mason, J. H., Li, W. & Liu, X. Comprehensive review of chromium deposition and poisoning of solid oxide fuel cells (SOFCs) cathode materials. *Renew. Sustain. Energy Rev.* **134**, 110320 (2020).
32. Mao, J. et al. Progress in metal corrosion mechanism and protective coating technology for interconnect and metal support of solid oxide cells. *Renew. Sustain. Energy Rev.* **185**, 113597 (2023).
33. Zhu, K. et al. Electrophoretic deposition of Mn–Co–Cu spinel coating enhancing high oxidation resistance and Cr inhibition of SUS430 interconnectors for Solid Oxide Cell. *Int. J. Hydrog. Energy* **179**, 151689 (2025).
34. Lenka, R. K., Patro, P. K., Sharma, J., Mahata, T. & Sinha, P. K. Evaluation of $La_{0.75}Sr_{0.25}Cr_{0.5}Mn_{0.5}O_3$ protective coating on ferritic stainless steel interconnect for SOFC application. *Int. J. Hydrog. Energy* **41**, 20365–20372 (2016).
35. Sun, Z. et al. $CuMn_{1.8}O_4$ protective coatings on metallic interconnects for prevention of Cr-poisoning in solid oxide fuel cells. *J. Power Sources* **378**, 125–133 (2018).
36. Molin, S. et al. Microstructural and electrical characterization of Mn-Co spinel protective coatings for solid oxide cell interconnects. *J. Eur. Ceram. Soc.* **37**, 4781–4791 (2017).
37. Aphale, A. et al. Synthesis and Stability of $Sr_xNi_yO_z$ Chromium Getter for Solid Oxide Fuel Cells. *J. Electrochem. Soc.* **165**, F635 (2018).
38. Ding, D., Li, X., Lai, S. Y., Gerdes, K. & Liu, M. Enhancing SOFC cathode performance by surface modification through infiltration. *Energy Environ. Sci.* **7**, 552–575 (2014).
39. Chen, Y. et al. A robust fuel cell operated on nearly dry methane at 500 °C enabled by synergistic thermal catalysis and electrocatalysis. *Nat. Energy* **3**, 1042–1050 (2018).
40. He, F. et al. Conformal high-entropy oxide coatings enable fast and durable surface oxygen reactions. *Joule* **9**, 101957 (2025).
41. Park, K. et al. Water-mediated exsolution of nanoparticles in alkali metal-doped perovskite structured triple-conducting oxygen electrocatalysts for reversible cells. *Energy Environ. Sci.* **17**, 1175–1188 (2024).
42. Hong, T., Brinkman, K. S. & Xia, C. Barium carbonate nanoparticles as synergistic catalysts for the oxygen reduction reaction on $La_{0.6}Sr_{0.4}Co_{0.2}Fe_{0.8}O_{3-\delta}$ solid-oxide fuel cell cathodes. *ChemElectroChem* **3**, 805–813 (2016).
43. Han, X. et al. Utilizing high entropy effects for developing chromium-tolerance cobalt-free cathode for solid oxide fuel cells. *Adv. Funct. Mater.* **33**, 2304728 (2023).
44. Witte, R. et al. High-entropy oxides: an emerging prospect for magnetic rare-earth transition metal perovskites. *Phys. Rev. Mater.* **3**, 034406 (2019).
45. Cheng, J., Navrotsky, A., Zhou, X.-D. & Anderson, H. U. Thermochemistry of $La_{1-x}Sr_xFe_{3-\delta}$ solid solutions ($0.0 \le x \le 1$, $0.0 \le \delta \le 0.5$). *Chem. Mater.* **17**, 2197–2207 (2005).
46. Yeh, J.-W. Recent progress in high-entropy alloys. *Ann. Chim. Sci. Matér.* **31**, 633–648 (2006).
47. Yang, Y. et al. A novel facile strategy to suppress Sr segregation for high-entropy stabilized $La_{0.8}Sr_{0.2}MnO_{3-\delta}$ cathode. *J. Power Sources* **482**, 228959 (2021).
48. Gao, Y. et al. A medium entropy cathode with enhanced chromium resistance for solid oxide fuel cells. *J. Eur. Ceram. Soc.* **43**, 2002–2012 (2023).
49. Li, Z. et al. High-entropy perovskite as a high-performing chromium-tolerant cathode for solid oxide fuel cells. *ACS Appl. Mater. Interfaces* **14**, 24363–24373 (2022).
50. Li, Z. et al. High-entropy cathodes with Cr and CO_2 tolerance via the combination of $Ba_{0.5}Sr_{0.5}Co_{0.8}Fe_{0.2}O_{3-\delta}$ and Nd, Ni, Zr ternary doping for both oxygen ion and proton conducting solid oxide fuel cells. *Adv. Compos. Hybrid. Mater.* **8**, 87 (2024).
51. Wei, B., Chen, K., Zhao, L., Lu, Z. & Jiang, S. P. Chromium deposition and poisoning at $La_{0.6}Sr_{0.4}Co_{0.2}Fe_{0.8}O_{3-\delta}$ oxygen electrodes of solid oxide electrolysis cells. *Phys. Chem. Chem. Phys.* **17**, 1601–1609 (2015).
52. Saqib, M. et al. Transition from perovskite to misfit-layered structure materials: a highly oxygen deficient and stable oxygen electrode catalyst. *Energy Environ. Sci.* **14**, 2472–2484 (2021).

53. Zhang, Y. et al. Thermal-expansion offset for high-performance fuel cell cathodes. *Nature* **591**, 246–251 (2021).
54. Liu, Z. et al. Synergistic dual-phase air electrode enables high and durable performance of reversible proton ceramic electrochemical cells. *Nat. Commun.* **15**, 472 (2024).
55. Richter, J., Holtappels, P., Graule, T., Nakamura, T. & Gauckler, L. J. Materials design for perovskite SOFC cathodes. *Monatsh. Chem. Chem. Mon.* **140**, 985–999 (2009).
56. Yang, Z., Yang, C., Jin, C., Han, M. & Chen, F. $Ba_{0.9}Co_{0.7}Fe_{0.2}Nb_{0.1}O_{3-\delta}$ as cathode material for intermediate temperature solid oxide fuel cells. *Electrochem. Commun.* **13**, 882–885 (2011).
57. Shen, L., Du, Z., Zhang, Y., Dong, X. & Zhao, H. Medium-entropy perovskites $Sr(Fe_{\alpha}Ti_{\beta}Co_{\gamma}Mn_{\zeta})O_{3-\delta}$ as promising cathodes for intermediate temperature solid oxide fuel cell. *Appl. Catal. B Environ.* **295**, 120264 (2021).
58. Zhu, F., He, F., Xu, K. & Chen, Y. Enhancing the oxygen reduction reaction activity and durability of a double-perovskite via an A-site tuning. *Sci. China Mater.* **65**, 3043–3052 (2022).
59. Zhang, Y. et al. Enhanced oxygen reduction kinetics of IT-SOFC cathode with $PrBaCo_2O_{5+\delta}/Gd_{0.1}Ce_{1.9}O_{2-\delta}$ coherent interface. *J. Mater. Chem. A* **10**, 3495–3505 (2022).
60. Chen, Y. et al. A highly efficient multi-phase catalyst dramatically enhances the rate of oxygen reduction. *Joule* **2**, 938–949 (2018).
61. Zhou, W., Jin, W., Zhu, Z. & Shao, Z. Structural, electrical and electrochemical characterizations of $SrNb_{0.1}Co_{0.9}O_{3-\delta}$ as a cathode of solid oxide fuel cells operating below 600 °C. *Int. J. Hydrog. Energy* **35**, 1356–1366 (2010).
62. Wang, J. et al. A broad stability investigation of Nb-doped $SrCoO_{2.5+\delta}$ as a reversible oxygen electrode for intermediate-temperature solid oxide fuel cells. *J. Electrochem. Soc.* **163**, F891 (2016).
63. Pang, S. et al. A-site cation deficiency tuned oxygen transport dynamics of perovskite $Pr_{0.5}Ba_{0.25-x}Ca_{0.25}CoO_{3-\delta}$ oxide for intermediate temperature solid oxide fuel cells. *Ceram. Int.* **45**, 14602–14607 (2019).
64. Lu, F. et al. Heterostructured simple perovskite nanorod-decorated double perovskite cathode for solid oxide fuel cells: highly catalytic activity, stability and CO_2-durability for oxygen reduction reaction. *Appl. Catal. B Environ.* **249**, 19–31 (2019).
65. Pang, S. et al. The role of A-site cation size mismatch in tune the catalytic activity and durability of double perovskite oxides. *Appl. Catal. B Environ.* **270**, 118868 (2020).
66. Qi, H., Cheng, M., Zhang, T., Liu, D. & Tu, B. Investigation of surficial and interfacial properties of $BaCo_{0.4}Fe_{0.4}Zr_{0.1}Y_{0.1}O_{3-\delta}$ cathode directly on yttria-stabilized zirconia electrolyte for solid oxide fuel cell. *Int. J. Hydrog. Energy* **46**, 36652–36662 (2021).
67. Liu, D. et al. B-site La, Ce, and Pr-doped $Ba_{0.5}Sr_{0.5}Co_{0.7}Fe_{0.3}O_{3-\delta}$ perovskite cathodes for intermediate-temperature solid oxide fuel cells: effectively promoted oxygen reduction activity and operating stability. *J. Power Sources* **494**, 229778 (2021).
68. Yang, Q. et al. A high-entropy perovskite cathode for solid oxide fuel cells. *J. Alloys Compd.* **872**, 159633 (2021).
69. Zhuang, Z. et al. Reversely trapping atoms from a perovskite surface for high-performance and durable fuel cell cathodes. *Nat. Catal.* **5**, 300–310 (2022).
70. Zhou, X., Yang, C., Yang, C., Li, J. & Chi, B. Self-assembled cathode induced by polarization for high-performance solid oxide fuel cell. *J. Mater. Chem. A* **11**, 1785–1792 (2023).
71. Xu, K. et al. An efficient construction of nano-interfaces for excellent coking tolerance of cermet anodes. *Mater. Today* **79**, 28–35 (2024).
72. He, F. et al. A highly oxygen reduction reaction active and CO_2 durable high-entropy cathode for solid oxide fuel cells. *Appl. Catal. B Environ. Energy* **355**, 124175 (2024).
73. Jung, W. & Tuller, H. L. Investigation of surface Sr segregation in model thin film solid oxide fuel cell perovskite electrodes. *Energy Environ. Sci.* **5**, 5370–5378 (2012).
74. Koo, B. et al. Sr segregation in perovskite oxides: Why it happens and how it exists. *Joule* **2**, 1476–1499 (2018).
75. Chen, K. & Jiang, S. P. Surface segregation in solid oxide cell oxygen electrodes: phenomena, mitigation strategies and electrochemical properties. *Electrochem. Energy Rev.* **3**, 730–765 (2020).
76. Pan, Z. et al. Experimental and thermodynamic study on the performance of water electrolysis by solid oxide electrolyzer cells with Nb-doped Co-based perovskite anode. *Appl. Energy* **191**, 559–567 (2017).
77. Chen, T. et al. High performance solid oxide electrolysis cell with impregnated electrodes. *Electrochem. Commun.* **54**, 23–27 (2015).
78. Zhang, M.-Y., Tian, Y.-F., Zou, L., Pu, J. & Chi, B. Synergistic enhancement of electrochemical performance in reversible solid oxide cells via deficiency-induced oxygen vacancy and nanoparticle generation. *Rare Met.* **44**, 264–274 (2025).
79. Wu, X. et al. Promotion of $Ca_3Co_4O_{9+\delta}$ oxygen electrode by in-situ exsolution of nanoparticles for solid oxide cells. *Int. J. Hydrog. Energy* **50**, 1246–1254 (2024).
80. Fang, C. et al. An active and durable air electrode with self-generated nanoparticles decorated on the surface for reversible oxygen-ionic ceramic electrochemical cells. *J. Mater. Chem. A* **12**, 7932–7942 (2024).
81. Lin, Q. et al. Improved $La_{0.8}Sr_{0.2}MnO_{3-\delta}$ oxygen electrode activity by introducing high oxygen ion conductor oxide for solid oxide steam electrolysis. *Int. J. Hydrog. Energy* **49**, 616–624 (2024).
82. Taniguchi, S. et al. Degradation phenomena in the cathode of a solid oxide fuel cell with an alloy separator. *J. Power Sources* **55**, 73–79 (1995).
83. Horita, T. et al. Determination of Chromium Concentration in Solid Oxide Fuel Cell Cathodes: (La,Sr)MnO3 and (La,Sr)FeO3. *Electrochem. Solid-State Lett.* **12**, B146–B149 (2009).
84. Jiang, S. P., Zhang, J. P., Apateanu, L. & Foger, K. Deposition of chromium species at Sr-doped $LaMnO_3$ electrodes in solid oxide fuel cells. I. Mechanism and kinetics. *J. Electrochem. Soc.* **147**, 4013–4022 (2000).
85. Wang, K. & Fergus, J. W. The effect of transition-metal doping on chromium deposition at Pt/YSZ cathode interfaces. *J. Electrochem. Soc.* **157**, B1008–B1011 (2010).
86. Ni, N., Wang, C. C., Jiang, S. P. & Skinner, S. J. Synergistic effects of temperature and polarization on Cr poisoning of $La_{0.6}Sr_{0.4}Co_{0.2}Fe_{0.8}O_{3-\delta}$ solid oxide fuel cell cathodes. *J. Mater. Chem. A* **7**, 9253–9262 (2019).
87. Key, C. et al. Methods to quantify reactive chromium vaporization from solid oxide fuel cell interconnects. *J. Electrochem. Soc.* **161**, C373 (2014).
88. Ebbinghaus, B. B. Thermodynamics of gas phase chromium species: the chromium oxides, the chromium oxyhydroxides, and volatility calculations in waste incineration processes. *Combust. Flame* **93**, 119–137 (1993).

Acknowledgements

Y.C. acknowledges the National Natural Science Foundation of China (22179039), the Introduced Innovative R&D Team of Guangdong (2021ZT09L392), Guangdong Basic and Applied Basic Research Foundation (2024A1515010448), the Fundamental Research Funds for the Central Universities (2022ZYGXZR002), Zijin Mining Group Co., Ltd (5405-ZC-2023-00008), and the Pearl River Talent Recruitment Program (2019QN01C693).

Author contributions

Y.C. conceived and supervised the project. F.Z. performed material characterizations and conducted all electrochemical tests. K.X., Y.L., and L.C. assisted in the material preparation. Y.X. and F. Hu assisted in material characterizations. F.Z., F. He, and X.Z. conducted data analysis.

All authors discussed the results and contributed to the writing of the paper.

Competing interests
The authors declare no competing interests.

Additional information
Supplementary information The online version contains supplementary material available at https://doi.org/10.1038/s41467-026-69338-8.

Correspondence and requests for materials should be addressed to Yu Chen.

Peer review information *Nature Communications* thanks the anonymous reviewers for their contribution to the peer review of this work. A peer review file is available.